Flow Measurement and Instrumentation 60 (2018) 171–184

Contents lists available at ScienceDirect

Flow Measurement and Instrumentation

journal homepage: www.elsevier.com/locate/flowmeasinst

# On the estimation of free-surface turbulence using ultrasonic sensors

G. Zhang[a], D. Valero[b,*,1], D.B. Bung[b,2], H. Chanson[a,3]

[a] Dept. of Hydraulic Engineering, School of Civil Engineering, The University of Queensland, Brisbane, QLD 4072, Australia
[b] Hydraulic Engineering Section, FH Aachen University of Applied Sciences, Bayernallee 9, Aachen 52066, Germany

ARTICLE INFO

*Keywords:*
Acoustic displacement meter
Free-surface dynamics
Wave
Power spectra
Air-water flows
Stepped spillway

ABSTRACT

Accurate determination of free-surface dynamics has attracted much research attention during the past decade and has important applications in many environmental and water related areas. In this study, the free-surface dynamics in several turbulent flows commonly found in nature were investigated using a synchronised setup consisting of an ultrasonic sensor and a high-speed video camera. Basic sensor capabilities were examined in dry conditions to allow for a better characterisation of the present sensor model. The ultrasonic sensor was found to adequately reproduce free-surface dynamics up to the second order, especially in two-dimensional scenarios with the most energetic modes in the low frequency range. The sensor frequency response was satisfactory in the sub-20 Hz band, and its signal quality may be further improved by low-pass filtering prior to digitisation. The application of the USS to characterise entrapped air in high-velocity flows is also discussed.

## 1. Introduction

Most common environmental flows are turbulent free-surface flows, transporting all sorts of waves ranging from the small-scale capillary waves to the breaking waves of the sea, which can be several metres in scale. While the free surface of a liquid in equilibrium is plane, under the action of a perturbation it will move from equilibrium, propagating this motion through the domain due to gravity and surface tension [36]. Despite major efforts (among others: [21,13,42,58]), understanding of free-surface turbulence is not available, becoming a bottleneck in many environmental applications. Although true relation between water turbulence properties and free-surface oscillations is not yet disclosed, such a relationship seems to exist [13,22,58,68–70]. A study of the turbulence properties of the free-surface may help understanding the processes happening beneath, shedding light on mass, momentum and heat transfer across gas-liquid interfaces. Additionally, the existence of a free-surface modifies the flow characteristics beneath, which also interact non-linearly with the free-surface [28,63,68]. Near the free-surface, turbulence anisotropy, altogether with shear reduction, seems to be a common feature in most studies [18,22,24]. Roussinova et al. [56], following the previous study of Nezu [46], suggested that the free-surface behaves as a “weak wall” where normal velocity fluctuations are countered by surface tension. Gualtieri and Gualtieri [20] conceptualized the free-surface interaction with turbulence to predict gas-transfer rates. Murzyn and Chanson [43] suggested that free-surface oscillations are linked to the turbulent kinetic energy per unit volume. Roussinova et al. [56] also observed that presence of a free-surface can yield secondary flows within the water body, which is in agreement with the hypothesis resulting of the study of Tamburrino and Gulliver [62]. Guo and Shen [22] illustrated the surface blockage effect and the vanishing of the shear stress and, later, Guo and Shen [23] studied the complex effect of waves on turbulence underneath. Recently, Nichols et al. [48] proposed a simple model for free-surface dynamics that may help in future to link the surface kinematics to the underlying complex turbulence phenomenon. Zhong et al. [77] found evidence of super-streamwise vortices, previously observed by Gulliver and Halverson [21], existing universally as free-surface coherent structures occurring in open channel flows.

Many processes can originate free-surface perturbations. Some studies have been conducted in the past, relating the external air flow effect to the generation of waves in the sea [27,29,39,74]. Yet free-surface can be also perturbed by other causes. Schvidchenko and Pender [60] found that the bursting phenomenon, contributing to sediment transport, generates eddies reaching the free-surface. This is in agreement with the previous study of Schvidchenko and Pender [59] who noticed that relative flow depth affects the erosion process; which

* Correspondence to: Research Group of Hydraulics in Environmental and Civil Engineering (HECE), University of Liège, Chemin des Chevreuils, 1, building B52/3 floor +1, 4000 Liège, Belgium.
*E-mail address:* valero@fh-aachen.de (D. Valero).
[1] ORCID: 0000-0002-7127-7547.
[2] ORCID: 0000-0001-8057-1193.
[3] ORCID: 0000-0002-2016-9650.

https://doi.org/10.1016/j.flowmeasinst.2018.02.009
Received 15 November 2016; Received in revised form 5 February 2018; Accepted 11 February 2018
Available online 13 February 2018

was later observed and further explained by the numerical study of Chang and Constantinescu [6]. Similarly, Dabiri [13] showed that the free-surface deformation may be strongly correlated to the normal surface vorticity produced in a vertical shear layer, showing also how simultaneously the presence of a free-surface alters its structure. Thus, not only turbulence may affect the free-surface but also the free-surface can affect the turbulence. Similarly, Roy et al. [57] observed that processes taking place on a gravel bed could reach the free-surface (megabursts). Savelsberg [58] found that free-surface roughness is linked to the sub-surface turbulence. Guo and Shen [22] numerically studied the free-surface roughness resulting from the isotropic turbulence generated underneath the free-surface, concluding that motion of the free-surface is composed of propagating waves and turbulence generated roughness. Horoshenkov et al. [25] noticed evidence of waves produced by turbulence generated over rough sediment surfaces, which showed considerably different phase velocity – frequency relation than common gravity waves. Johnson and Cowen [30] were able to estimate flow discharges based on free-surface turbulent properties.

Waves have been also observed in the non-aerated region of spillway flows [1,15,66–68,75]. Valero and Bung [66] observed the dynamics of these waves in the inception point location and Valero and Bung [67] described the different types of waves, pointing out the role of air-water friction in the wave generation when high velocity flows take place. Another clear evidence of free-surface turbulence - due to the underlying hydrodynamic processes - can be observed in hydraulic jumps [10], which have been also investigated previously using ultrasonic sensors [5,69]. Hydraulic jump quasi-periodic features were first pointed out by Nebbia [45], in a phenomenon amplified by the changing jump due to erosion. Since then, dynamic processes resulting from the high velocity flow impacting the slower velocity downstream flow have attracted researchers' interest. Long et al. [38] used imaging techniques; Mossa [40] and Mossa et al. [41] used a pressure transducer, a resistance probe and a video camera to study periodic and quasi-periodic phenomenon inside the jump. During the last decade, free-surface fluctuations of hydraulic jump rollers were studied mainly by means of ultrasonic sensors, yielding a greater insight on the overall flow turbulence. Koch and Chanson [34] first used ultrasonic sensors to study undular and breaking bores. Additional studies using ultrasonic sensors [35,43,5,71,72] provided deeper insight on free-surface turbulence in stationary hydraulic jumps. Additionally, this technique has been also applied to high velocity spillway flows [3,4]. Its capability to study both aerated and non-aerated regions has been shown [66] obtaining characteristic flow depths, its oscillations and waves frequencies in stepped spillway flows [4]; however, larger deviation can be expected in the study of the aerated region [15]. Other studies have related ultrasonic measurement to characteristic aeration levels: $\overline{h}_{50} - \overline{h}_{60}$ for a slightly aerated bubbly column [9], $\overline{h}_{60} - \overline{h}_{80}$ for the hydraulic jump roller flow [35] and $\overline{h}_{75}$ for aerated spillway flows [4]; with $\overline{h}_X$ the mean water depth associated with a mean air concentration $\overline{C} = X$ (%). Murzyn and Chanson [43] and Chachereau and Chanson [5], suggested otherwise that the ultrasonic measurement in a hydraulic jump might correspond to a thin region below the upper free-surface region but always over the air-water shear layer.

Albeit different measurement techniques are available, ultrasonic sensors may be of special interest in many applications because of their robustness and non-intrusive nature. Traditional point gauge allows static measurements usually at an accuracy of 0.1 mm. Wave gauges can additionally perform dynamic measurements, similarly to ultrasonic sensors, but are subject to temperature changes within the water body and also flow perturbation or sensors interference can happen. Naturally, sensors interference can also happen between ultrasonic sensors and temperature effect must be contemplated, but non-intrusiveness can represent an advantage. Main benefits of other techniques can be met by ultrasonic sensors, but its performance has to be carefully assessed to ensure reliable non-intrusive measurements of free-surface profiles, free-surface fluctuations, free-surface correlation time scales, free-surface wave celerity and frequencies [15,4,43,5,67]. Additionally, how the footprint relates to the measurement has not been still assessed.

The promising future of other acoustic techniques for velocity [37,44,55,64] and free-surface determination [26,33,47] motivates this research which aims to assess the performance of a pulse-echo ultrasonic sensor for common environmental flows. Different common environmental flows have been studied both by means of ultrasonic sensors and a high-speed camera in the following sections. The manuscript is structured as follows: performance of the ultrasonic sensor has first been studied in dry conditions in Section 3. In Section 4.2, a 2D wave flume investigation is presented. Section 4.3 presents study of the ultrasonic sensor accuracy in the non-aerated region of a spillway; which represents a 3D wavy open channel flow, more challenging than the counterpart subcritical flows commonly studied. Section 4.4 presents some comments on the ultrasonic sensors' performance and capabilities for aerated flows which is further completed by the analysis presented in Section 4.5 for the air content estimation. Finally, Section 5 collects the main conclusions of the presented study.

## 2. Experimental setup and instrumentation

### 2.1. Instrumentation

The primary instrumentation used in the present investigation included three cylindrical microsonic™ mic+130 ultrasonic sensors (USS) for analogue free-surface measurements plugged to a computer through a HBM™ QuantumX 840A amplifier. The sensors utilise a pulse-echo principle and operate at a transducer frequency of 200 kHz (note that this frequency is related to resolution but not to sampling rate). The acoustic sensing range is 0.2–2.0 m with corresponding resolutions between 0.18 mm and 0.57 mm (specified by the sensors' manufacturer), and a "blind zone" is defined for 0–0.2 m. The size of the detection zone was between 0.05 m and 0.15 m, yielding a minimum expected precision of 1.1% (for wavelengths greater than the detection zone size). Errors due to temperature drift are internally compensated. The sensors are IP 67 rated and were well suited for the laboratory operating conditions. Note that only one sensor model was tested herein.

For comparison, data were recorded by a Phantom™ M120 high-speed video camera synchronised with the USS sensors via an in-house Python script. The camera was capable of recording at up to 730 fps at a resolution of 1920 by 1200 pixels (throughput: 1.6 Gpx/s), and it was possible to increase the frame rate by reducing the image resolution. Two 500 W halogen lights were customarily placed to achieve visually homogenous illumination across the scene. The free-surface profiles were deduced from the digital image sequences using various image processing techniques depending on the flow type of each experiment. The camera was sampled at 100 fps at a resolution of 1920 by 1200 pixels for all experiments. The sample rate was selected as a compromise between precision and storage requirements.

Synchronisation of sensors was achieved by simultaneously triggering the USS and camera sample clocks. When the USS clock fires, a Python script sends a trigger to the camera clock by calling the Windows application programming interfaces (Win32 API). Any misalignment due to software delay (typically less than 0.1 s) was compensated using a cross-correlation technique, corrected to the nearest sample (i.e. 0.02 s). The data acquisition software were Catman v3.3 (HBM™) and DaVis v8.1 (LaVision™) for the USS and camera respectively. The USS and camera were respectively sampled at 50 Hz and 100 Hz for 30 s during all experiments. The higher camera sampling rate helps to facilitate better matching between the signals. The sampling parameters were chosen herein to achieve a balance between accurate signal reconstruction and hardware capacity (especially the camera). It is acknowledged that a minimum of 5000–10,000 samples would be desirable to characterise turbulence properties up to the second order (i.e. variance) (e.g. [31,11]).

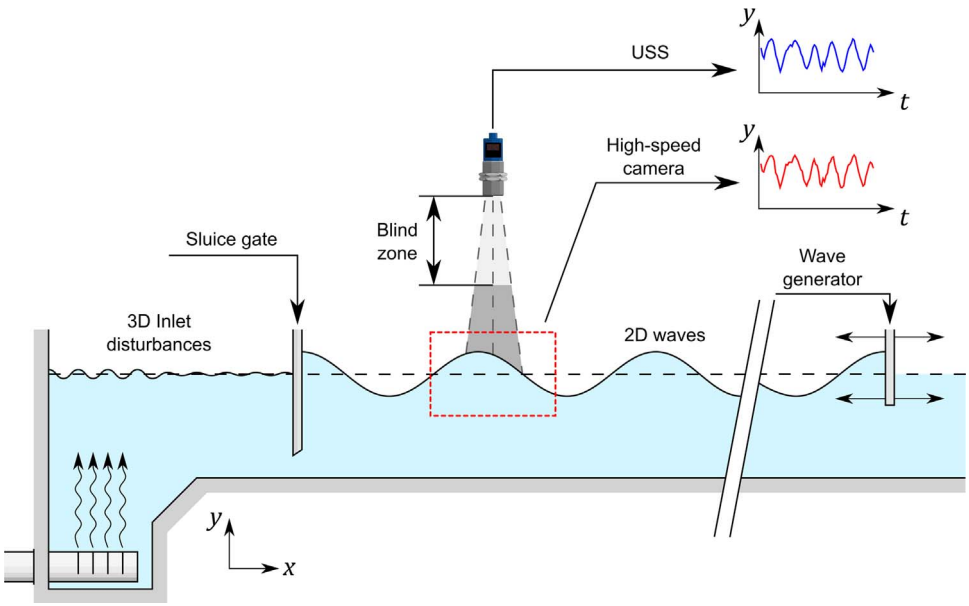


**Fig. 1.** Sketch of the setup in the 2D wave experiment.

Detailed void fraction measurements were performed with a dual-tip optical fibre probe (A2 Photonic Sensors™). The data were derived from the leading tip signal, sampled for 45 s at 1 MHz, which was considerably above the minimum recommended sample rate for similar techniques [16].

### 2.2. Experimental facilities

Present investigations were undertaken in relatively large-size physical models in the FH Aachen Hydraulics Laboratory (Aachen, Germany). The model discharge was delivered through a closed conduit and was regulated by a frequency regulator (Grundfos™ blueflux). An electromagnetic flow meter (Krohne™ WATERFLUX 3100 W) was used to measure the discharge, with an expected error of 0.3%.

The first experiment, for validation purposes, was performed in a wave flume of dimensions 0.58 m wide by 0.80 m high and 12 m long. A sketch of the facility is shown in Fig. 1. The discharge was supplied from an upstream intake and drained through the gaps between several rows of flap gates located at the downstream end of the flume. A discharge of 0.015–0.020 $m^3/s$ was maintained in the flume such that the water depth was visually constant, prior to any waves being generated. The first train of waves was generated by manually operating a flat plate at the downstream end of the flume at approximately 0.5 Hz. The waves propagated upstream and were reflected by a sluice gate located near the upstream end of the channel. The stimulus was applied continuously to produce a range of complex and uncontrolled waves with characteristic heights between 0.005 m and 0.20 m, observed synchronously by both the camera and USS. An average water depth of approximately 0.40 m was maintained during this process.

The high-speed video camera was set up beside the channel with a field of view measuring 0.138 m by 0.86 m (landscape). The halogen lights were placed such that the water surface was naturally enhanced when observed from the camera, and a dark background was set to improve contrast. The first USS sensor was mounted approximately 0.10 m inside the sidewall and 0.40 m above the water surface, with a measuring zone of approximately 0.10 m in diameter. A second USS sensor was mounted in symmetry with the primary sensor about the channel centreline for checking the two-dimensionality of the waves. It was found that mismatches between the USS and high-speed camera data were minimised when waves were approximately two-dimensional. However, small discrepancies may arise due to surface tension and wall effects.

Further tests were performed in a 1V:2H (26.6°) stepped spillway model to study the feasibility of USS in scenarios with increased free-

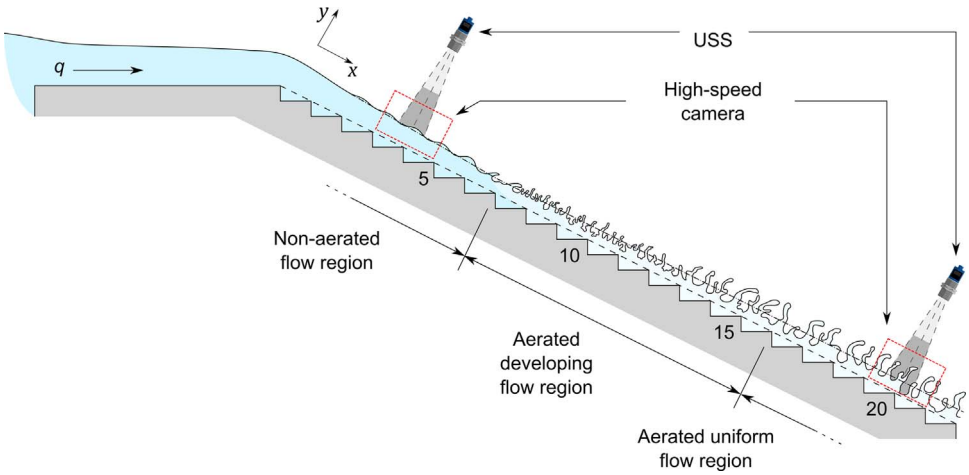


**Fig. 2.** Stepped spillway experimental configuration in the non-aerated and aerated measurements.

**Table 1**
Experimental flow conditions for the 3D free-surface roughness experiment in the stepped spillway model.

| Location | $q$ ($m^2$/s) | Width (m) | Slope, $\theta$ (°) | Re | Remarks |
|---|---|---|---|---|---|
| Step 4 | 0.090 | 0.5 | 26.6 | $9.0\times10^4$ | Clear water skimming |
| | 0.110 | | | $1.1\times10^5$ | flow |
| Step 20 | 0.090 | 0.5 | 26.6 | $9.0\times10^4$ | Aerated skimming |
| | 0.110 | | | $1.1\times10^5$ | flow |

surface geometric complexity in high velocity supercritical flows. A sketch of the facility is shown in Fig. 2. The model was 0.50 m wide and had a total drop height of 1.74 m, lined with 0.06 m × 0.12 m (rise × run) flat impervious steps ($\theta$ = 26.6°). The chute inflow was controlled by a 1.0 m long broad-crested weir with discharge delivered by the same system as for the wave flume. Free-surface fluctuations were sampled with a rail-mounted USS at approximately 0.07 m inside the sidewall. The high-speed video camera was mounted beside the channel with a field-of-view of about two step cavities wide. The experimental flow conditions are summarised in Table 1, with Reynolds numbers (Re) ranging from 9x10$^4$ to 1.1x10$^5$.

## 3. Sensor calibration and signal characterisation

### 3.1. Presentation

The USSs were first tested in dry conditions to observe their capabilities and signal characteristics. The voltage responses of each USS was examined by placing a perpendicular solid plastic surface at different distances from the sensor. The voltage–distance relationship was linear throughout the measuring range of the sensor. A "blind zone" and a "far field" were respectively identified close to and away from the sensor as per Fig. 3. The standard deviation of each static measurement was interpreted as the measurement uncertainty, which remained approximately constant over the full detectable range. The results showed no preferential measuring distance despite the maximum detected deviation (around 1 mm) seemed to increase with distance (Fig. 3). Information on Fig. 3 was sampled over 30 s.

The footprint of the USS is shown in Fig. 4. This footprint was measured by fixing the sensor and repeatedly introducing a plate at different distances away from the transducer and recording the distance from the centreline at which the USS detected the obstacle. The USS signal changes in a space of around 1 mm. The sensing cone shown in Fig. 4 spreads with distance at an angle of 4°. The sensor allows internal adjustments of the detection zone (options: "normal/slight"), although no significant difference was found between the options (Fig. 4). Difficulty in detecting steeper waves by similar sensors was noted in several previous studies [15,34,4]. The sensitivity of the sensing error to surface slope ($\alpha$) variations is examined in Fig. 4 (right). It was observed that outliers did not occur for surface slopes flatter than 13.5°.

The temperature dependence of the USSs was investigated by undertaking long measurements of 12 h at a sample rate of 1 Hz. In Fig. 5, only the data for the first 6 h are shown for clarity. Notably, most significant changes in the sample mean were observed during the first hour. Consequently, a minimum warm-up period of 1 h as advised by the manufacturer after which calibration shall be required prior to data acquisition.

### 3.2. Sample rate, aliasing and noise

The USS operates by measuring the time lag between the emitted and reflected ultrasound pulses. The pulses are emitted at a pre-established interval to ensure that all meaningful echoes are captured before a new pulse is broadcast. The shortest pulse interval determines the maximum frequency that needs to be resolved by the data acquisition (DAQ) system of which the sampling frequency must be appropriately chosen. The Nyquist sampling theorem [49,50,61] requires this to be equal to or greater than twice the maximum frequency present in the signal (i.e. Nyquist frequency). This minimum sampling frequency is known as the Nyquist rate. Failure to satisfy the Nyquist criterion will result in a higher frequency signal with frequency $f$ manifesting as a lower frequency component with an apparent frequency equalling $|f_s - f|$ where $f_s$ is the sampling frequency. As such, the original signal can no longer be reconstructed by low pass filtering without distortion and this is referred to as aliasing [50].

The effects of sampling rate and analogue filtering were first investigated by examining the USS signal power spectral densities plotted in Fig. 6. The data were sampled with the USS facing a fixed flat surface perpendicular to the sensor centreline. The signal mean was removed prior to computing the power spectral density functions. The oversampled power spectral density function at 1200 Hz (Fig. 6 black/grey lines) shows a steep roll-off above 20 Hz and an isolated peak at 60 Hz. The latter peak likely arose from the connected electronics, as the local main frequency was 50 Hz. The USS signal was therefore approximately bandlimited up to 20 Hz (i.e. cut-off), and that a minimum sampling rate of 50 Hz is recommended to minimise aliasing distortion. Note that a minimum sampling rate of 10 times the Nyquist frequency (i.e. 250 Hz for a sampling rate of 50 Hz) may be required for accurate waveform reproduction [2].

The use of analogue low-pass filtering prior to digitisation helps prevent aliasing distortion. Fig. 6 (black dash) shows a USS signal digitised at 50 Hz post low-pass filtering (Butterworth with a cut-off frequency of 20 Hz). Comparison with the oversampled power spectral density function at 1200 Hz (Fig. 6 black line) reveals a good reproduction of the spectral components up to the Nyquist frequency. The built-in analogue Butterworth filter was effective at removing aliases

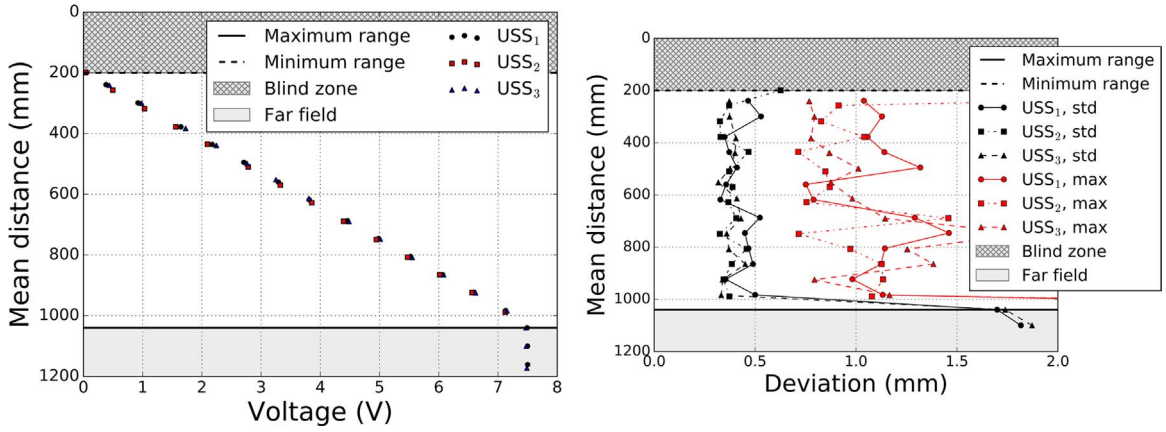


**Fig. 3.** Linear calibration curve (left), standard deviation (std) and maximum value (max) of a static measurement at different distances from the USS (right) without any signal filtering.

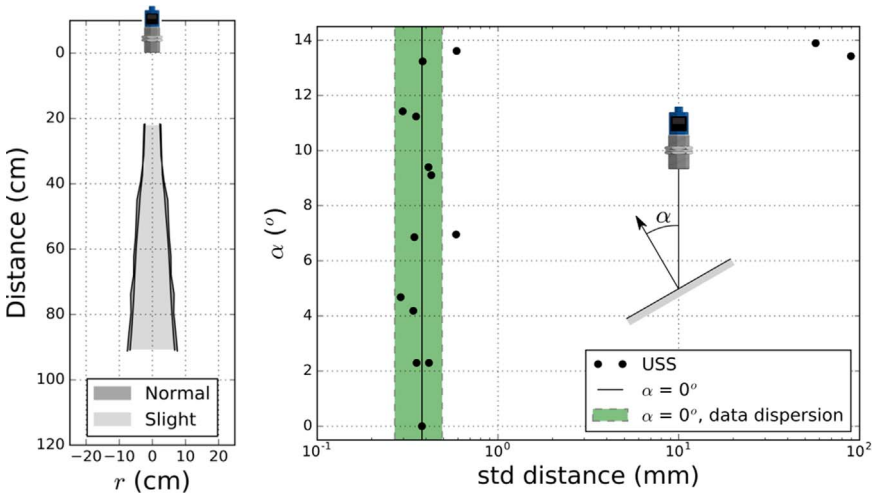


**Fig. 4.** (Left) Footprint of a USS measured at the laboratory (present model). Objects are detected when placed within the sensor's detection radius, which is a function of the surface roughness. (Right) Standard deviation dependence on the surface slope.

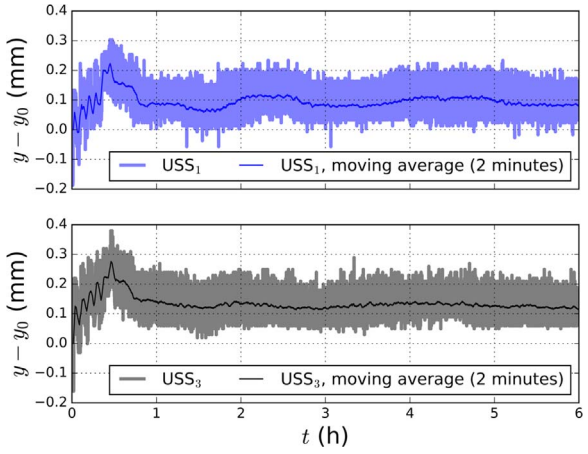


**Fig. 5.** Long time record of USS signals for two different sensors. Temperature has significant effects on sensor data during the first hour. The initially measured distance ($y_0$) is subtracted to the recording.

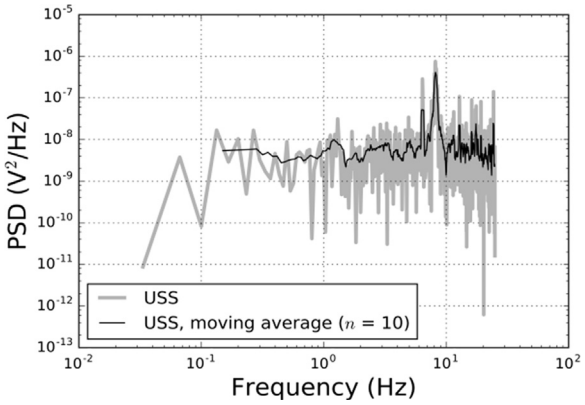


**Fig. 7.** Typical noise power spectral density function (PSD) of a USS signal. Sampling rate: 50 Hz. Sampling Duration: 30 s.

from frequencies above the Nyquist frequency (25 Hz) without significantly degrading the passband (0 – 20 Hz). Note that low-pass filtering may not always be required on account of the much lower USS frequency response above 20 Hz. The filter implementations also differ amongst analogue to digital conversion (ADC) systems. For simplicity, all analogue filters are disabled herein.

A review of Fig. 6 indicates that a minimum sampling rate of 50 Hz may be required. The typical USS noise power spectral density function sampled at this rate, with all filters disabled, is shown in Fig. 7. The data revealed an aliased peak at 10 Hz due to power fluctuations, which may not be important if the signal-to-noise ratio is large. The power spectral density function was approximately white (i.e. equal intensity in all frequencies) up to the Nyquist frequency (25 Hz) due to the combined effects of temperature, surface-characteristics and intrinsic electrical noise of the system.

### 3.3. Detectable frequencies and uncertainty involved in the wave amplitude determination

Any USS sensor has a limited response time which represents a limitation when measuring high frequencies. In order to investigate the performance of the USS at those frequencies, experiments with a

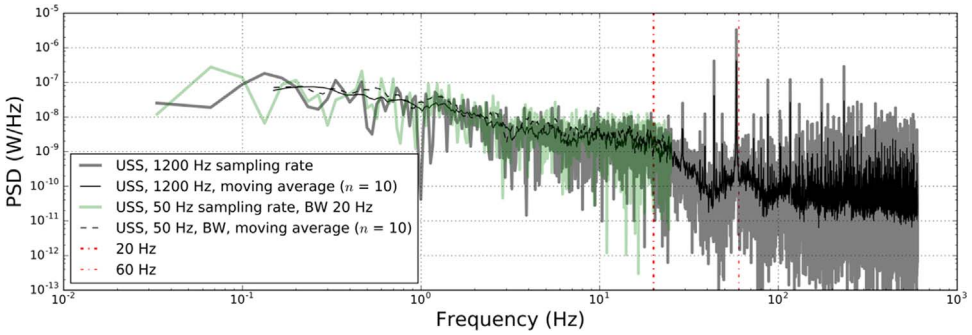


**Fig. 6.** Effects of sampling rate and analogue filtering on USS signal power spectral density function (PSD). BW for Butterworth filtered signals.

vibrating plate were conducted.

A PVC plate was fixed over an aluminium bar (isel™, universalprofile PU50), whose combination of elasticity modulus ($E$ = 70 GPa), density (1.22 kg/m), inertias (in both transversal axis, $I_x$ = 10.99 cm$^4$ and $I_y$ = 2.81 cm$^4$) and length (up to 3 m) allowed study of frequencies below 30 Hz. The bar was fixed to a solid and massive metal structure so that a cantilever was resulted with the plastic plate close to the bar extremity. Two USS sensors were placed at 0.50 m above the plastic plate and were separated by 0.20 m to avoid interference. The bar was shortened iteratively, thereby increasing the stiffness of the system. For each length investigated, the bar was stimulated with a single impact producing oscillations with amplitudes significantly above those of the USS noise. Two bars were used, profiting from both transversal inertias to cover a wider range of frequencies. The high-speed camera was employed using significantly higher sample rates (over ten times the bar frequency) to obtain the real frequency of the vibrating system. The frequencies in both cases were estimated by counting zero-crossings over the first second after the impact.

A close correspondence is observed between the camera and USS frequencies up to 20 Hz, while frequencies above 20 Hz were increasingly underreported by the USS. To gain further insight, a simple case where a plate oscillates as described by the sine equation is considered:

$$h'(t) = A \sin(2\pi f t + \varphi) \tag{1}$$

where $A$ is the amplitude, $f$ the frequency of the oscillation, $t$ the time and $\varphi$ the initial phase shift. If the speed of the plate is considerably smaller than the speed of the sound ($v \ll c$), then it is reasonable to assume that the sensor will see the object at every sampling time as static, i.e.: as a fixed plate at a different height each time.

For different values of $f$, Eq. (1) can be used to generate a new signal. A hundred different frequencies with a hundred different initial phase shifts (randomly initialised) have been used to render synthetic signals with $N$ = 100 no. of complete periods. Zero-crossings can be counted in a similar manner to that for the vibrating plate tests, thus recovering the same original frequency. This signal can also be reproduced by subsampling, as an USS naturally does due to its limited sampling. A best match was found for $f_{sample}$ = 43 Hz, which corresponds to a cut-off frequency of 21 Hz, corroborating with the considerations in the previous subsections. In Fig. 8, the theoretical response of the USS is shown as 'modelled'. It must be noted that the expected decay of the frequency detected by the USS agrees with the experimental observations. For frequencies below 21 Hz the response of the USS is satisfactory. In the case of a small $N$, the under-sampled frequencies ($f > 21$ Hz) would show larger scatter while the lower frequencies still fit perfectly to the 1:1 line.

It is also of interest to analyse how under-sampling would affect the

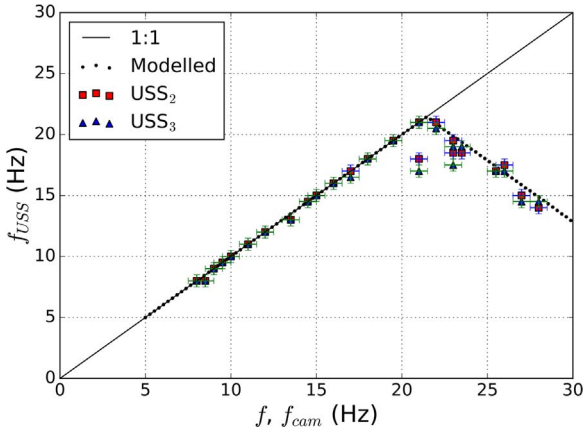


**Fig. 8.** Frequency detected by the ultrasonic sensor ($f_{USS}$) against frequency detected with the high-speed camera ($f_{cam}$) and modelled frequency ($f$).

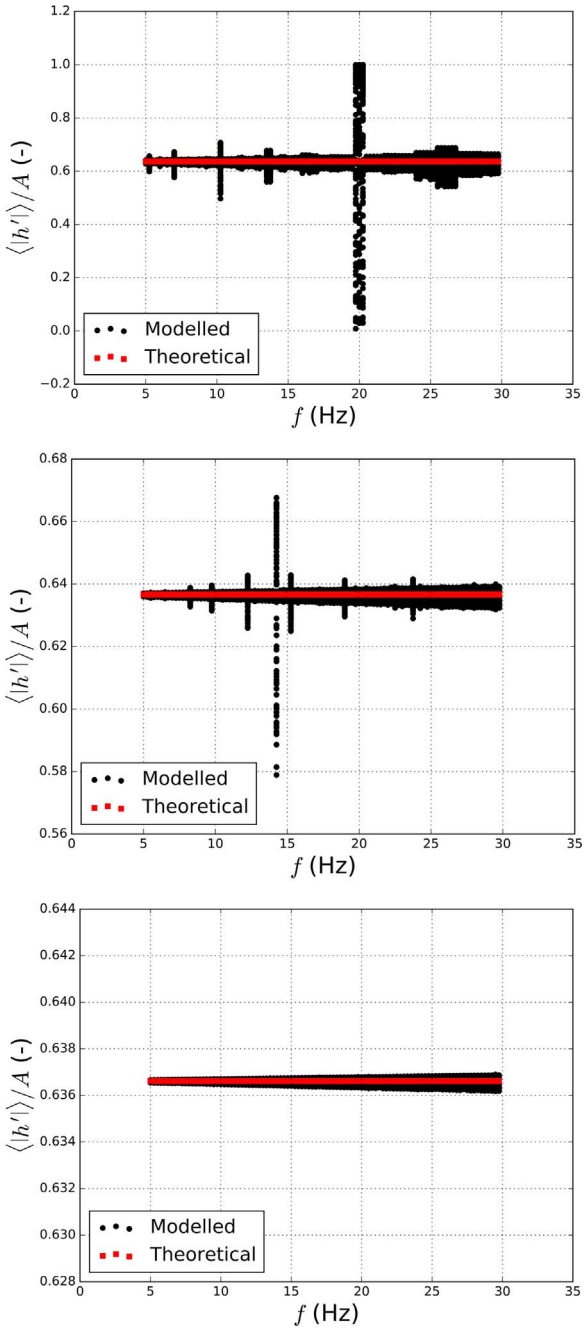


**Fig. 9.** Uncertainty in the absolute value of the fluctuation depending on the frequency of the measured oscillating process. Top: $N$ = 10; middle: $N$ = 100; bottom: $N$ = 1000.

prediction of wave amplitudes for different wave frequencies. The expected absolute value of the fluctuation ($\langle|h'|\rangle$) resulting from this under-sampling is shown in Fig. 9. Despite a finite number of frequencies, the uncertainty grows linearly with the oscillation frequency. It has also been observed that the widths of these bounds are reduced by increasing the number of sampled waves ($N$). Thus, the uncertainty associated to under-sampling can be compensated by a larger number of sampled processes.

The standard deviation (std) of a sine wave is given by:

$$std(h') = A \quad /\sqrt{2} \tag{2}$$

which can be obtained from the sampled synthetic signals. A pseudoamplitude can be recovered by emulating the amplitude which might be obtained from the USS sampling:

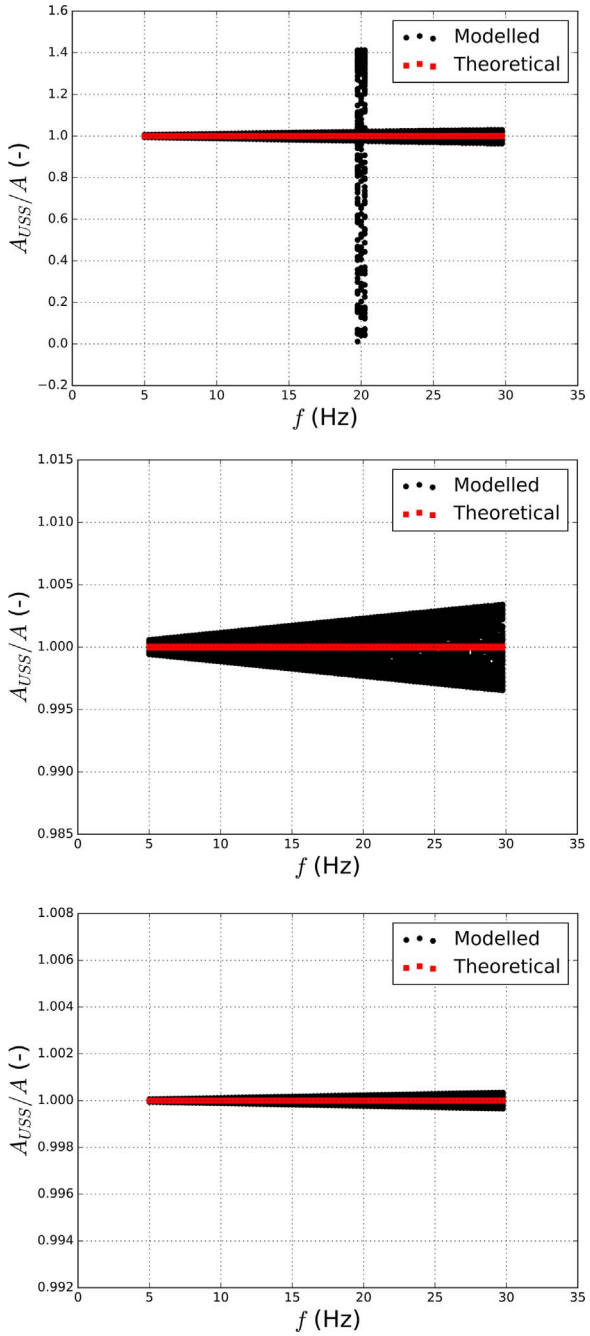


**Fig. 10.** Pseudoamplitude resulting from USS under-sampling. Top: $N = 10$; middle: $N = 100$; bottom: $N = 1000$. Note the different range of the amplitude axis.

$$A_{USS} = std(h') \quad \sqrt{2} \tag{3}$$

The resulting pseudoamplitude $A_{USS}$ is shown in Fig. 10. It can be observed, similarly to Fig. 9, that for small sampling durations a considerably large uncertainty band appears at around 20 Hz. Similar to the absolute amplitude, incrementing the number of sampled events reduces the uncertainty bound.

## 4. USS measurements in turbulent flows

### 4.1. General considerations

The microsonic™ mic+130 ultrasonic sensor has a detection cone with radii ranging approximately between 0.02 m and 0.1 m, depending on the object distance from the sensor (Fig. 4, left). The actual detection zone further depends on material acoustic properties and surface roughness characteristics. The distance reported by the USS is also dependent on the spatial distribution of intensities of the emitted beamlet, which can be characterised by a complex pattern but is always strongest along the sensor axis. Therefore, the most robust measurements are taken along the central axis. In first approximation, a roughened water surface may be understood as a set of piecewise linear elemental surfaces on which the ultrasound reflection is specular. The echoes picked up by the USS comprise series of signals reflected by the individual surface elements which are orthogonal to the direction of propagation of the emitted beam. When multiple echoes are present, preliminary tests (with arrangements of multiple objects at various depths) suggested that the USS strongly favoured the foreground signal (i.e. the first obstacle met by the echoes). Consequently, USS measurement over a rough water surface would result in a characteristic distance, determined by the integral of the signals reflected from the stationary phase points within the first half Fresnel zone of the acoustic signal, which may vary depending upon the instantaneous water surface geometry covered by the USS footprint (as opposed to the commonly expected average value).

In light of the above considerations, three test cases were established to investigate the validity of USS free-surface measurements in turbulent flows. The test cases were set up in the order of increasing surface geometry complexities. Detailed results pertaining to each case are presented in the following subsections.

### 4.2. Wave flume experiment

A wave flume was set up as an academic test of the USS sampling properties in absence of major three-dimensional effects. A description of the facility is provided in Section 2 (see Fig. 1). For meaningful comparisons between the signals, the free-surface must be delineated accurately from the camera data, the quality of which can be degraded by sources including suspended particles in water and light reflections at the water surface. To this end, a custom post-processing technique was developed which consisted of the following steps:

- Smooth the original image by convolving with 2D median filters with kernel sizes between 11 and 55 pixels, followed by visual quality checks;
- Convolve the smoothed image with a 1D central difference kernel, upon which a column-wise lookup was performed to locate a likely free surface, using the 90th percentile image gradient for each column as the criterion;
- Fit a least-squares sine wave to the estimated free-surface;
- Smooth the gradient image with a 1D Gaussian kernel centred around the fitted sine-wave;
- Perform a row-wise search of the free-surface based on an adaptive, percentile-based threshold calculated for each column, and smooth with a median filter.

Fig. 11 illustrates a typical sequence of high-speed camera images plotted at 5 s intervals. The numerically delineated free-surfaces are highlighted in red. Detailed visual examinations confirmed an excellent agreement between the visually and numerically identified free-surfaces (i.e. with uncertainties of up to a few pixels, of the same order of magnitude as the USS resolution of 0.18 mm).

Fig. 12 compares the water level fluctuations ($h'$) obtained with the USS to those delineated from high-speed camera footages. The camera data was extracted at the pixel location intersecting the USS centreline and subsampled at 50 Hz (so that both data have the same number of points). Qualitative inspection indicates a good agreement between the data. The USS experienced some difficulties reproducing the details around the wave peaks and troughs, because steeper water surfaces redirect ultrasound echoes away from the receiving area of the sensor. This also leads to an isolated peak at around 11–12 s, where the echo was barely detected by the sensor if at all.

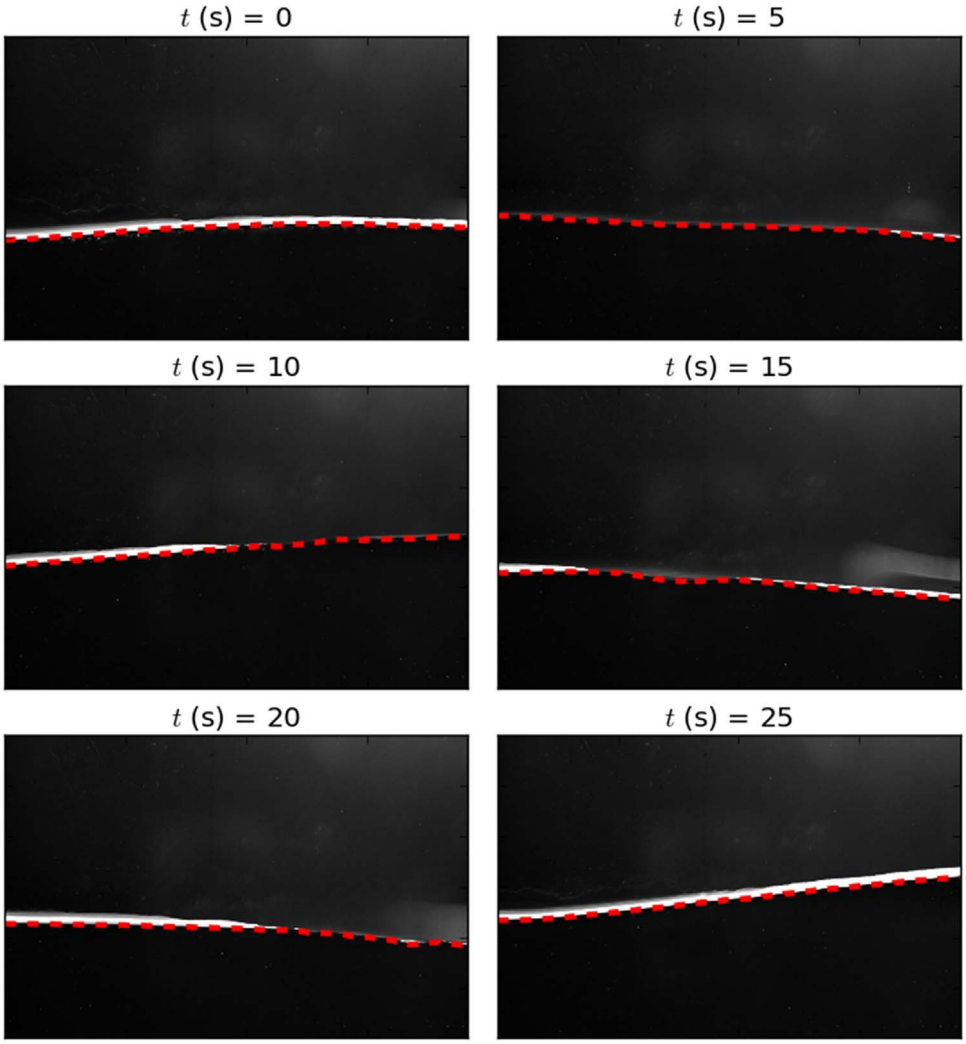


**Fig. 11.** Free-surface (red dashed line) delineation from high-speed camera images. Waves entering from both sides. (For interpretation of the references to color in this figure legend, the reader is referred to the web version of this article.)

In a number of fluid applications, the free-surface statistics up to the second order are usually of interest [13,15,22,25,30,4,43,48,5,58,67,71]. For this purpose, the quality of the USS data was inspected by comparing its power spectral density function and autocorrelation function to those of the camera images extracted signal (Fig. 13). Both signals were normalised by first subtracting the mean, then dividing by their respective standard deviations for ease of comparison. An assessment of the power spectral density functions shows that the USS was able to adequately reproduce the spectral characteristics of the fluctuating water surface. Most discrepancies appeared to involve the highest frequencies, which have powers approximately two orders of magnitudes lower than the most energetic spectral range (Fig. 13). The variance of both signals after conversion into physical units differed by a mere 0.25% (52.20 $mm^2$ vs 52.07 $mm^2$). The autocorrelation functions of both signals were practically indistinguishable (Fig. 13). The present evidences indicate that the USS is capable of reliably estimating second order statistics in the present exercise.

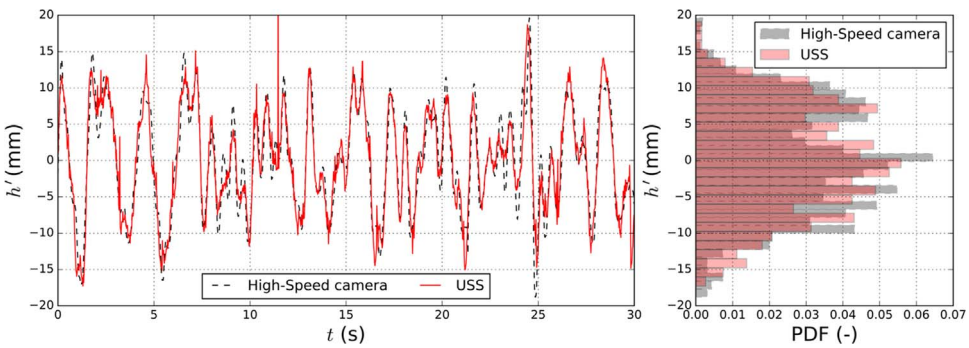


**Fig. 12.** Free-surface fluctuation ($h'$) in the 2D wave experiment, comparison between the USS and the high-speed camera processed signal. Temporal series (left) and PDF (right).

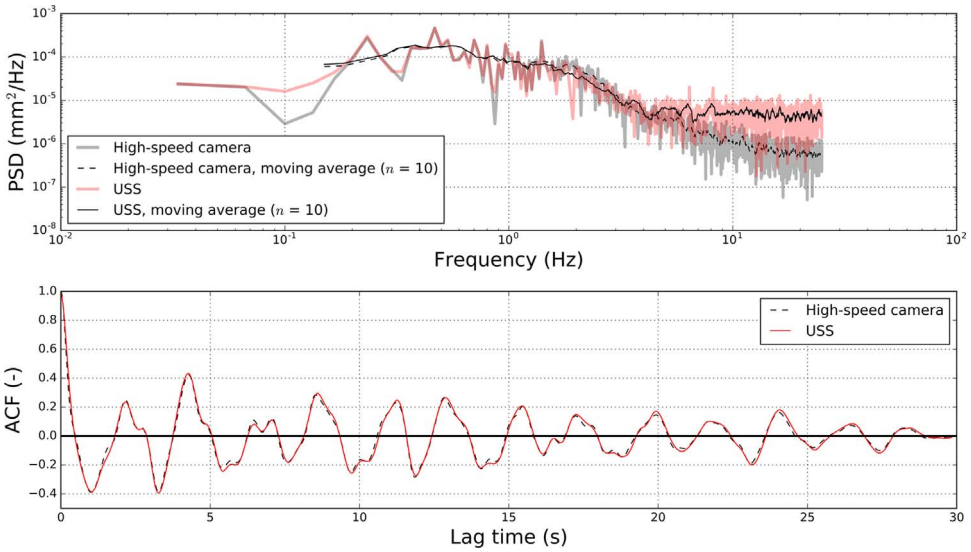


**Fig. 13.** Comparison of power spectral density (PSD, top) and autocorrelation function (ACF, bottom) between normalised USS and camera signals for the 2D wave experiment.

### 4.3. Non-aerated stepped spillway flow

The applicability of the USS in practical scenarios was investigated in a large-size stepped spillway model. The experimental setup is described in Section 2. The free-surface was extracted from the video frames using an image processing technique illustrated in Fig. 14(a) through (d), consisting of the following steps:

- Construct a gradient image by convolving the original image with a central difference kernel (Fig. 14(a));
- Estimate the water surface based on a thresholding technique, as used in the wave experiments (Fig. 14(b));
- Construct a difference image by subtracting a typical water surface luminance level from all pixels in the scene and smooth with a median filter;
- Smooth the difference image by a 10 pixels wide 2D Gaussian filter centred at the average level of the estimated water surface (Fig. 14(c));
- Locate the water surface by finding the maximum responses of the resultant image from the last step (Fig. 14(d)).

It was noted that occasional bright blobs arising from three-dimensional artefacts in the background could corrupt the algorithm. The likelihood of these events was deemed small enough so as to not produce a significant bias in the camera data.

Fig. 15 (left) shows a typical comparison of the free-surface fluctuations recorded with the USS with those extracted from the high-speed video image sequence at a streamwise location corresponding to the USS centreline. The corresponding probability density functions (PDF) of the water surface fluctuations are presented in Fig. 15 (right).

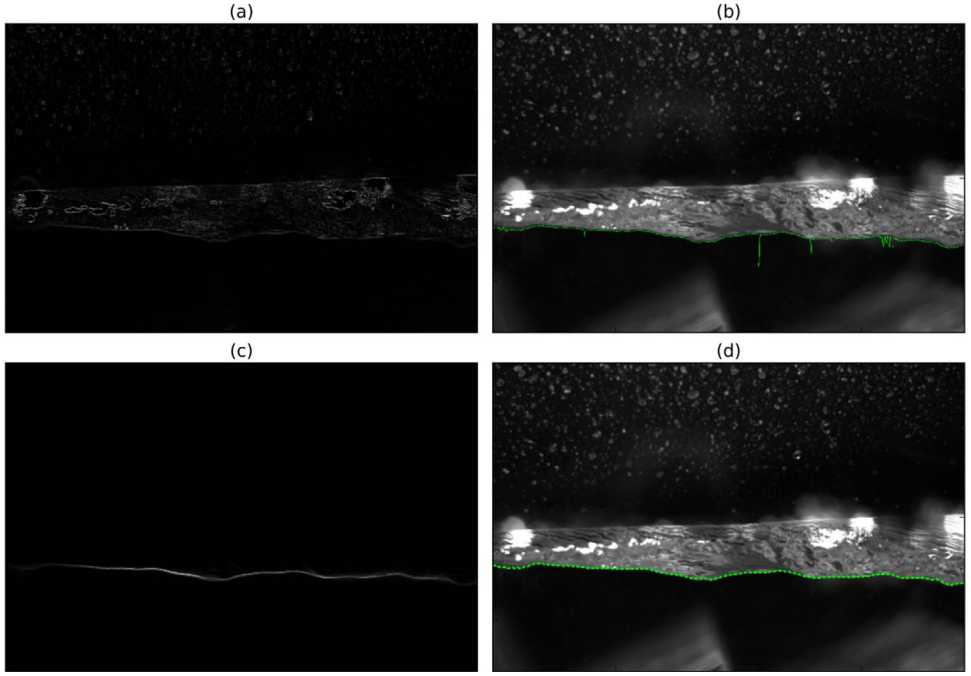


**Fig. 14.** Free-surface extraction from high-speed video camera images in non-aerated flow region, with flow direction from left to right – (a) gradient image; (b) estimated free-surface from gradient image (green dash); (c) filtered difference image; (d) extracted free-surface (green dash). Flow conditions: $q = 0.090\,\mathrm{m}^2/\mathrm{s}$, $\theta = 26.6°$, step 4 (edge), flow direction from left to right.

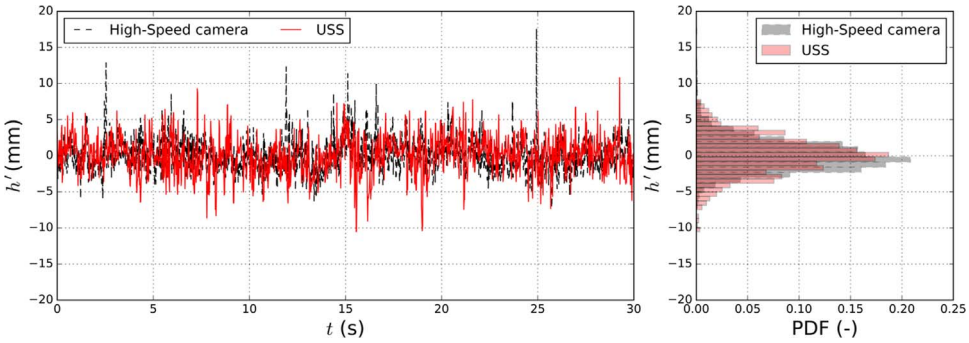


**Fig. 15.** Free-surface fluctuation ($h'$) in the stepped spillway non-aerated region, comparison between the USS and the high-speed camera processed signal. Temporal series (left) and PDF (right).

Note that the video was sampled at twice the frequency of the USS (100 Hz vs 50 Hz). It was seen that the most significant fluctuations (low frequency oscillations) of the free-surface were reproduced satisfactorily in both signals, while the local details oftentimes differ. The PDFs of both signals appear to be Gaussian-shaped centred at zero. This spread of the flow depth measured could be interpreted as a characteristic size of the surface waves, as previously discussed [4,67]. The standard deviations of the USS and camera data were found to be 2.69 mm and 2.13 mm respectively. The difference could be caused by the three-dimensional nature of the free-surface fluctuations and by the camera technique subjected to side-wall effects.

Fig. 16 compares the one-sided autocorrelation functions and power spectral density functions between the normalised USS and camera signals. Note that the camera signal was subsampled at 50 Hz to facilitate comparison. The autocorrelation functions for both signals (Fig. 16, bottom) appear to be similar, and a significant periodicity of 2.5 s may be identified from both signals which correspond to the peak at approximately 0.4 Hz observable from their respective power spectral density functions (Fig. 16, top). Note that the autocorrelation function of a periodic signal is also periodic with the same period. While the power spectral density functions for both signals appeared to be qualitatively consistent, the three-dimensional nature of the free-surface couple with the spikes in either signal contributed to some differences in the distribution of signal power over the spectral range. The slow decay of the power spectral density functions over the highest spectral range could be consequential of aliasing error caused by signal frequencies above the Nyquist frequency. This reflects the broad-spectrum nature of the underlying process, highlighting that a higher sampling rate might be preferable to fully resolving the free-surface fluctuations.

Contrarily to the case study presented in Section 4.2, maximum correlation between USS and camera datasets dropped drastically to 0.141 which could be explained by the three-dimensional nature of the flow in a spillway. Defining the integral length scale in the traversal direction ($L_z$) as [52]:

$$L_z = \int_0^\infty f(z)dz \tag{4}$$

being $f(z)$ the autocorrelation function for the velocity and $z$ the transverse coordinate; it seems reasonable to assume:

$$f(z) = e^{-\frac{z}{L_z}} \tag{5}$$

Although Eq. (5) is a simplification (e.g. it does not allow computation of Taylor microscale given the wrong curvature at $z = 0$, see Pope [52], but resembles other experimental curves), it satisfies Eq. (4) in a simple way and allows approximation of the expected correlation at a given distance (for a larger $z$ values, prediction seems reasonable). Having a mean flow depth ($\overline{h}$) of around 4 cm and assuming $L_z \sim \overline{h}$ following the studies of Roy et al. [57] and Johnson and Cowen [30], for simplicity $L_z = \overline{h}$; the correlation function taking the distance between USS and camera measurements may not be bigger than $f\left(\frac{7}{4}\right) = 0.174$, consequently giving an upper value for the maximum correlation between both signals (0.141).

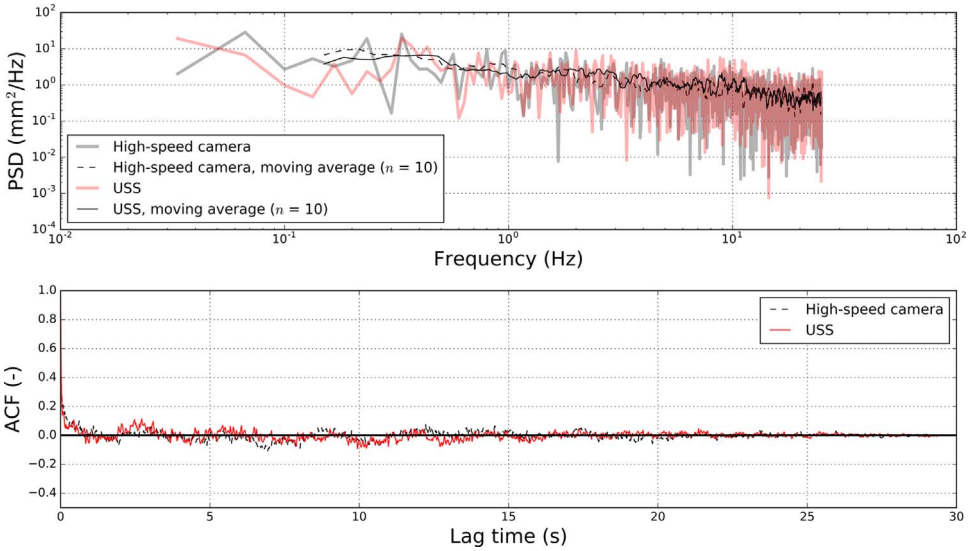


**Fig. 16.** Comparison of power spectral density (PSD, top) and autocorrelation function (ACF, bottom) between normalised USS and camera signals for the stepped spillway non-aerated region.

### 4.4. Aerated stepped spillway flow

The performance of the USS was further investigated in the fully-developed region on a stepped chute. In this region, the spillway flow is characterised by an intense air-entrainment process and strong turbulent mixing. The USS has been previously employed by several authors during investigations of such type of flows (e.g. [9] at a plunging breaker; [43,5,72,71] in hydraulic jumps; [67] in smooth spillways; [4,15,66] in stepped spillways). The penetration properties of the ultrasonic beam in the aerated flow region, however, remain inconclusive based on several previous reports [35,4,43,5,9], and are likely a complex function of the sensor model, beam characteristics and flow conditions. Meanwhile, the canonical free-surface is equally ill-defined in this region. For these reasons, a simple gradient-based technique was used to extract a characteristic free-surface from the images:

- Construct a gradient image by convolving a Gaussian-blurred original image with a Sobel kernel [19];
- Perform a row-wise search to locate a free-surface based on an adaptive threshold;
- Remove any spurious point using a 2D median filter of 39 px in diameter.

Four examples of free-surfaces extracted from the high-speed video camera images are shown in Fig. 17. The results were reasonably robust despite the simplistic technique, and the extracted free-surface conforms generally well to the typical human perception of a free-surface. Note that occasional occurrences of large bright spots due to droplet projections in the background may result in spurious points unable to be removed by filtering alone. Such noise will contribute to an increased variance in the data, although the likelihood of these events is small enough that their aggregate effects are deemed to be insignificant.

The USS and camera signals in the aerated flow region are compared in Fig. 18 (left), and their respective histograms shown in Fig. 18 (right). Occasionally, large droplets are projected into the USS dead zone and these data were nulled out by setting a threshold at $\pm$ 3 times the standard deviation of the USS signal. An examination of the waveforms indicates some similarities, despite a greater level of variation in the USS data. The histograms shown in Fig. 18 (right) are skewed to the left (standardized skewness for the data from the camera: -0.40; USS: -0.59), suggesting a sampling bias towards foreground flow features (i.e. droplet projection) due to the nature of the pulse-echo principle. The standard deviations of the USS and camera data were found to be 10.79 mm and 7.77 mm respectively.

The autocorrelation functions and power spectral density functions of the normalised USS and camera signals are calculated and plotted in Fig. 19. Both autocorrelation functions were essentially flat while lacking any significant periodicities. Correspondingly, the power spectral density functions were approximately uniform up to the Nyquist frequency (25 Hz) similar to that of a white noise. The observation implies that water surface fluctuations in the aerated flow region encompasses a broad-spectrum of frequencies, and that the present sampling rate was insufficient to adequately resolve the process.

The maximum cross-correlation coefficient between USS and camera signals was around 0.145, again below the 0.174 approximated as a theoretical maximum despite the fact that the aerated region is much more complex than a normal open channel flow.

### 4.5. Discussion: USS signal CDF and void fraction profiles

In a free-surface aerated flow, the USS signal outputs provide a range of free-surface locations at a given section. The probability density function (PDF) of the USS signal describes the likelihood of a variable to take a certain value. Similarly, the cumulative density function (CDF) allows knowledge on the probability of that variable to remain below or equal to a given value. When all the air content is entrapped air, the free-surface CDF could be analogous to the time-averaged void fraction profile [67]. However, air bubbles beneath the free-surface can by no means be accounted with an USS, and this limitation must be kept in mind, as this is a common feature of high-velocity self-aerated flows [53,54,7,73]. Whereas bubbles cannot be detected, capability of the USS to measure the entrapped air was investigated. However, further understanding of the air-water flow structure is necessary to assess the behaviour of the sensor and, consequently, this study only aims to give a glimpse on “what is measured” with an USS when the flow is highly aerated, thus complementing the previous analysis for non-aerated flows.

In Fig. 20, the void fraction profiles at step edges 4 and 20 are shown, which correspond to sections discussed previously at 0.07 m from the sidewalls. The theoretical void fraction distributions of

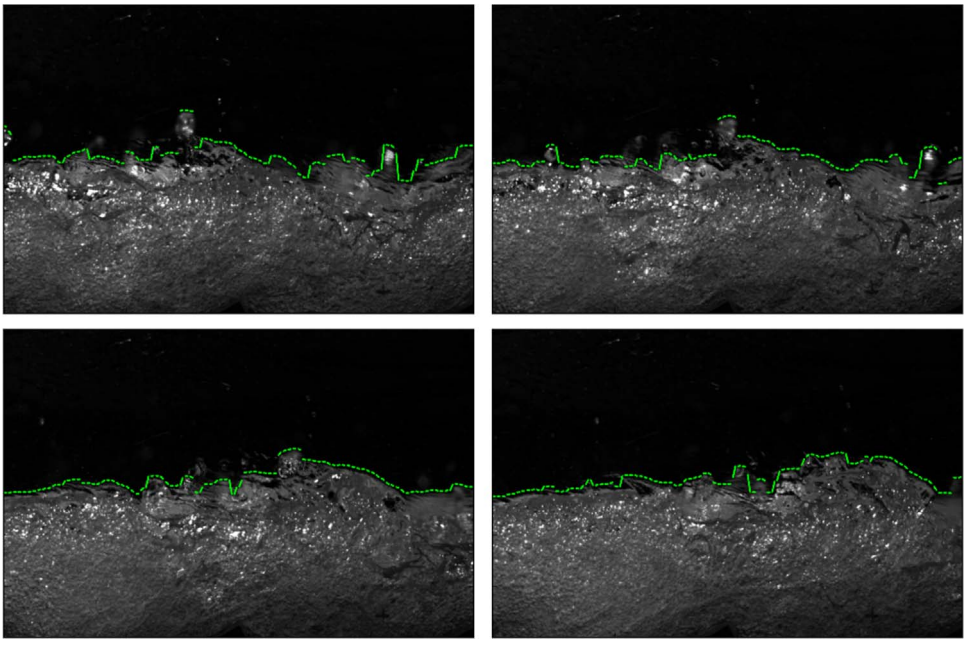

**Fig. 17.** Free-surface extraction in the aerated flow region. Flow conditions: $q = 0.110\,m^2/s$, $\theta = 26.6^\circ$, step 20 (edge). Flow from left to right.

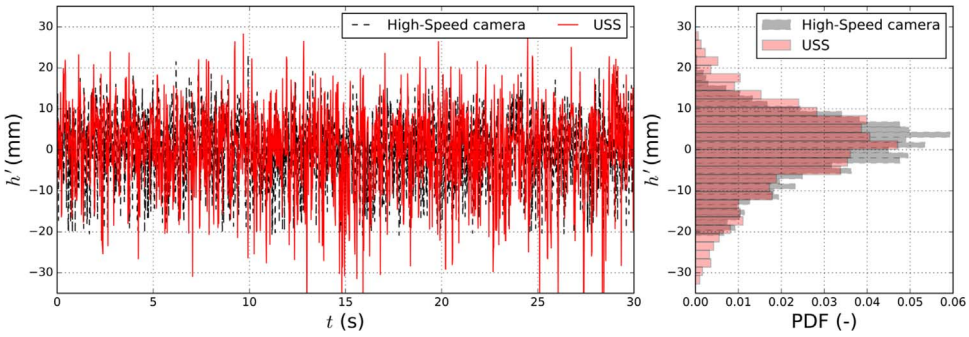


**Fig. 18.** Free-surface fluctuation ($h'$) in the stepped spillway aerated region, comparison between the USS and the high-speed camera processed signal. Time series (left) and PDF (right).

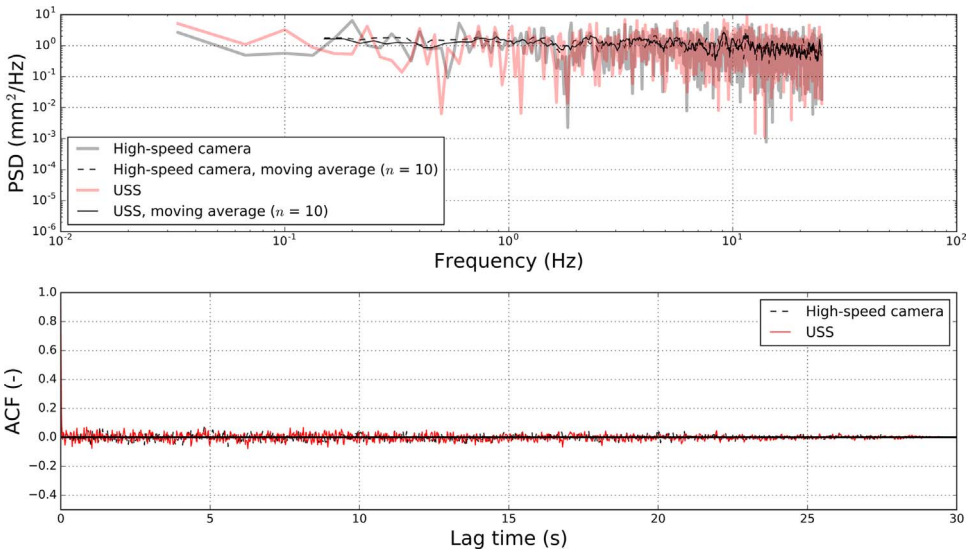


**Fig. 19.** Comparison of power spectral density (PSD, top) and autocorrelation function (ACF, bottom) between normalised USS and camera signals for the stepped spillway aerated region.

Chanson and Toombes [12] and Valero and Bung [67] are included in Fig. 20 for comparison, and all the data are presented in dimensionless form in terms of $\overline{h}_{50}$ (flow depth where $\overline{C} = 0.5$) and with $\overline{h}_{90}$ (flow depth where $\overline{C} = 0.9$) obtained with the optical fibre probe, in the non-aerated and the aerated regions respectively, following Zhang and Chanson [76].

A number of studies previously associated time-averaged USS data to different void fraction levels [35,4,43,5,9]. In the non-aerated region, the USS CDF data demonstrated similar accuracy to the optical fibre probe and theoretical profiles (see Fig. 20 left). In the aerated flow region, when bubbles are trapped inside the water flow, information on the void fraction profile are irreparably lost by the USS, as observed in Fig. 20 (right). Thereof, capability of the USS to better reproduce the free-surface roughness will determine up to which extent the entrapped air concentration can be reproduced and, consequently, as entrapped air and entrained air seem to be related [32,65], connection between

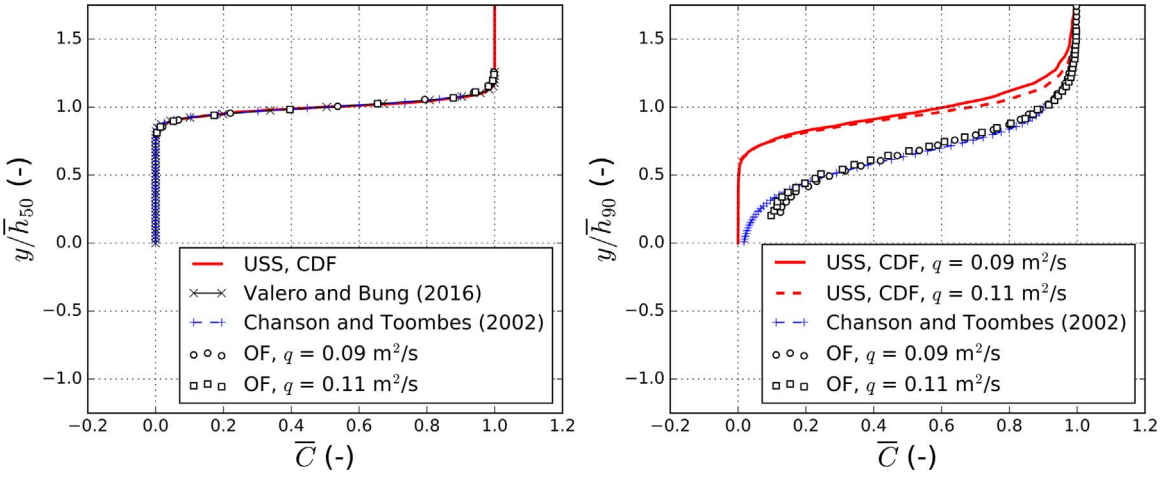


**Fig. 20.** Air concentration on the non-aerated region (left, step 4) and in the aerated region (right, step 20) measured both with an optical fibre (OF) probe and the USS at 7 cm from the wall.

USS measurement and total air concentration could be established. USS air concentration profile of Fig. 20 (right) resembles those of Killen [32] obtained with a specific conductivity probe (so-called probability probe). When the air content is predominant ($\overline{C} \approx 1$), the optical fibre and USS measurements converge. The optical fibre and USS data diverged with decreasing void fraction: for example, the USS reported $\overline{C} \approx 0.6$ at $y/h_{90} = 1$ (OF). Ideally, this was caused by air bubbles forming within the water roughness not being detected by the USS. The maximum penetration depth of the USS ($\overline{C} = 0.02 - 0.05$) corresponded approximately to $\overline{C} = 0.5\overline{C}(y) = 0.5$ according to the optical fibre data. This location has been suggested as a transition [51] in the air-water flow structure [14,17,32,76,8].

## 5. Conclusion

Ultrasonic sensors (USS) allow dynamic determination of the free-surface which, consequently, allows the estimation of free-surface turbulence properties. Herein the applicability of an ultrasonic pulse-echo sensor to turbulent free-surface flows was systematically investigated. An examination of the signal characteristics revealed satisfactory frequency responses in the sub-20 Hz band, while the signal quality may be improved by low-pass filtering prior to digitisation. A minimum sampling rate of 50 Hz is recommended in accordance with the sensor's dynamic capabilities.

The USS performances were tested by sampling synchronously with a Phantom M120 high-speed video camera in several turbulent free-surface flows in order of increasing complexity. The USS is capable of satisfactory reproduction of statistics up to the second order when the flow is essentially monophasic and two-dimensional, with dominant modes in the low frequency range (2D wave flume) (i.e. a 0.25% difference between USS and camera data variance, further to an excellent visual match). As the water surface fluctuations become more three-dimensional (e.g. high velocity clear water stepped chute flow), the USS is able to reproduce the most energetic modes as long as they are below the Nyquist frequency. The sampling bias of the ultrasound beamlets towards foreground signals becomes especially evident when the flow comprises an inhomogeneous mixture and the free-surface roughness is governed by highly three-dimensional processes (e.g. aerated stepped chute flow). In such cases the USS data should be at best interpreted as characteristics over the entire sampling surface, on account of its severely degraded applicability due to limitations of the sampling principle.

In highly turbulent flows (e.g. aerated spillway flow), the primary limitation of the USS is its limited frequency response. The broad-spectrum of time-scales in such processes cannot be adequately resolved from heavily aliased USS signals, and other instrumentations with higher sample rates are preferable (i.e. phase-detection probes). Applicability of the USS in these cases should be appraised on an individual basis, after a careful validation. Caution should be exercised when the data interpretation extends beyond time-averaged quantities. The USS capabilities to reproduce air transport were tested, showing that air concentration can be reproduced with similar accuracy to an optical fibre probe when all the air content is entrapped (i.e. no bubbly flow). In a fully aerated flow, the USS CDF data resembled Killen's [32] prediction for entrapped air but diverged significantly from the void fraction distribution determined using an optical fibre probe.

Overall, the present investigation demonstrated the capabilities as well as limitations of a USS in several types of turbulent flows via successful implementation of a synchronised USS and high-speed camera sampling system. It is important to note that the individual USS performance is a complex function of sensor model, surface properties, and flow characteristics, and that actual experimental conditions might be more challenging compared to common open channel flows studied in literature.

## Acknowledgements

The authors wish to acknowledge the support of the University of Queensland Graduate School International Travel Award (UQ-GSITA), of the 2017 Australia-Germany Joint Research Co-operation Scheme (Universities Australia) and the German Academic Exchange Service (DAAD, with financial support of the Federal Ministry of Education and Research BMBF). The authors also thank A2 Photonic Sensors for providing the optical fibre instrumentation.

## References

[1] H.O. Anwar, Discussion on: "self-aerated flows on chutes and spillways", J. Hydraul. Eng. 120 (6) (1994) 778–779.
[2] B.D. Bissett, Practical Pharmaceutical Laboratory Automation, CRC Press, 2003.
[3] D.B. Bung, Developing flow in skimming flow regime on embankment stepped spillways, J. Hydraul. Res. 49 (5) (2011) 639–648, http://dx.doi.org/10.1080/00221686.2011.584372.
[4] D.B. Bung, Non-intrusive detection of air–water surface roughness in self-aerated chute flows, J. Hydraul. Res. 51 (3) (2013) 322–329, http://dx.doi.org/10.1080/00221686.2013.777373.
[5] Y. Chachereau, H. Chanson, Free-surface fluctuations and turbulence in hydraulic jumps, Exp. Therm. Fluid Sci. 35 (2011) 896–909, http://dx.doi.org/10.1016/j.expthermflusci.2011.01.009.
[6] K. Chang, G. Constantinescu, Coherent structures in flow over two-dimensional dunes, Water Resour. Res. 49 (5) (2013) 2446–2460, http://dx.doi.org/10.1002/wrcr.20239.
[7] H. Chanson, Air bubble entrainment in free-surface turbulent shear flows, Academic Press, 1996.
[8] H. Chanson, Hydraulics of aerated flows: qui pro quo? J. Hydraul. Res. 51 (3) (2013) 223–243, http://dx.doi.org/10.1080/00221686.2013.795917.
[9] H. Chanson, S. Aoki, M. Maruyama, Unsteady air bubble entrainment and detrainment at a plunging breaker: dominant time scales and similarity of water level variations, Coast. Eng. 46 (2) (2002) 139–157, http://dx.doi.org/10.1016/S0378-3839(02)00069-8.
[10] H. Chanson, T. Brattberg, Experimental study of the air–water shear flow in a hydraulic jump, Int. J. Multiph. Flow. 26 (4) (2000) 583–607, http://dx.doi.org/10.1016/S0301-9322(99)00016-6.
[11] H. Chanson, M. Trevethan, C. Koch, Discussion on turbulence measurements with acoustic Doppler velocimiters, J. Hydraul. Eng. 134 (6) (2007) 883–887, http://dx.doi.org/10.1061/(ASCE)0733-9437(2008)134:6(883).
[12] H. Chanson, L. Toombes, Air-water flows down stepped chutes: turbulence and flow structure observations, Int. J. Multiph. Flow. 28 (11) (2002) 1737–1761, http://dx.doi.org/10.1016/S0301-9322(02)00089-7.
[13] D. Dabiri, On the interaction of a vertical shear layer with a free surface, J. Fluid Mech. 480 (2003) 217–232, http://dx.doi.org/10.1017/S0022112002003671.
[14] H. Falvey, Discussion on: bubbles and waves description of self-aerated spillway flow, J. Hydraul. Res. 45 (1) (2007) 142–144, http://dx.doi.org/10.1080/00221686.2007.9521755.
[15] S. Felder, H. Chanson, Air-water flows and free-surface profiles on a non-uniform stepped chute, J. Hydraul. Res. 52 (2) (2014) 253–263, http://dx.doi.org/10.1080/00221686.2013.841780.
[16] S. Felder, H. Chanson, Phase-detection probe measurements in high-velocity free-surface flows including a discussion of key sampling parameters, Exp. Therm. Fluid Sci. 61 (2015) 66–78, http://dx.doi.org/10.1016/j.expthermflusci.2014.10.009.
[17] S. Felder, H. Chanson, Air–water flow characteristics in high-velocity free-surface flows with 50% void fraction, Int. J. Multiph. Flow. 85 (2016) 186–195, http://dx.doi.org/10.1016/j.ijmultiphaseflow.2016.06.004.
[18] M.M. Gibson, W. Rodi, Simulation of free surface effects on turbulence with a Reynolds stress model, J. Hydraul. Res. 27 (2) (1989) 233–244, http://dx.doi.org/10.1080/00221688909499183.
[19] R.C. Gonzalez, R.E. Woods, S.L. Eddins, Digital Image Processing Using MATLAB, Pearson Prentice Hall, 2004 (ISBN: 0-13-008519-7).
[20] C. Gualtieri, P. Gualtieri, Turbulence-based models for gas transfer analysis with channel shape factor influence, Environ. Fluid Mech. 4 (2004) 249–271.
[21] J.S. Gulliver, M.J. Halverson, Measurements of large streamwise vortices in an open-channel flow, Water Resour. Res. 23 (1) (1987) 115–123.
[22] X. Guo, L. Shen, Interaction of a deformable free surface with statistically steady homogeneous turbulence, J. Fluid Mech. 658 (2010) 33–62, http://dx.doi.org/10.1017/S0022112010001539.
[23] X. Guo, L. Shen, Numerical study of the effect of surface waves on turbulence underneath. Part 1. Mean flow and turbulence vorticity, J. Fluid Mech. 733 (2013) 558–587, http://dx.doi.org/10.1017/jfm.2013.451.
[24] R.A. Handler, T.F. Swean, R.I. Leighton, J.D. Swearingen, Length scales and the energy balance for turbulence near a free surface, AIAA J. 31 (11) (1993) 1998–2007.
[25] K.V. Horoshenkov, A. Nichols, S.J. Tait, G.A. Maximov, The pattern of surface waves in a shallow free surface flow, J. Geophys. Res.: Earth Surf. 118 (3) (2013) 1864–1876, http://dx.doi.org/10.1002/jgrf.20117.
[26] K.V. Horoshenkov, T. Van Renterghem, A. Nichols, A. Krynkin, Finite difference time domain modelling of sound scattering by the dynamically rough surface of a turbulent open channel flow, Appl. Acoust. 110 (2016) 13–22, http://dx.doi.org/

10.1016/j.apacoust.2016.03.009.
[27] T. Hristov, S. Miller, C. Friehe, Dynamical coupling of wind and ocean waves through wave-induced air flow, Nature 422 (6927) (2003) 55–58, http://dx.doi.org/10.1038/nature01382.
[28] J.C.R. Hunt, J.M.R. Graham, Free-stream turbulence near plane boundaries, J. Fluid Mech. 84 (2) (1978) 209–235, http://dx.doi.org/10.1017/S0022112078000130.
[29] J. Janssen, The Interaction of Ocean Waves and Wind, Cambridge University Press, 2004.
[30] E. Johnson, E. Cowen, Schleiss, et al. (Ed.), Remote Monitoring of Volumetric Discharge based on Surface Mean and Turbulent Metrics. River Flow 2014, Taylor & Francis Group, London, 2014(ISBN 978-1-138-02674-2).
[31] R.I. Karlsson, T.G. Johansson, LDV measurements of higher-order moments of velocity fluctuations in a turbulent boundary layer.In: Proceedings of the 3rd International Symposium on Applications of Laser Anemometry to Fluid Mechanics, R.J. Adrian, D.F.G. Durao, F. Durst, H. Mishina, and J.H. Whitelaw (editors), 276-289, 1986.
[32] J.M. Killen, The Surface Characteristics of Self Aerated Flow in Steep Channels (Ph.D. Thesis), University of Minnesota, Minneapolis, MN, 1968.
[33] A. Krynkin, K.V. Horoshenkov, A. Nichols, S.J. Tait, A non-invasive acoustical method to measure the mean roughness height of the free surface of a turbulent shallow water flow, Rev. Sci. Instrum. 85 (11) (2014) 114902, http://dx.doi.org/10.1063/1.4901932.
[34] C. Koch, H. Chanson, Turbulence measurements in positive surges and bores, J. Hydraul. Res., IAHR 47 (1) (2009) 29–40, http://dx.doi.org/10.3826/jhr.2009.2954.
[35] S. Kucukali, H. Chanson, Turbulence measurements in the bubbly flow region of hydraulic jumps, Exp. Therm. Fluid Sci. 33 (1) (2008) 41–53, http://dx.doi.org/10.1016/j.expthermflusci.2008.06.012.
[36] L.D. Landau, E.M. Lifshitz, Fluid Mechanics. Course of Theoretical Physics, second edition, 6 Elsevier, Butterworth-Heinemann, 1987.
[37] X. Leng, H. Chanson, Unsteady velocity profiling in bores and positive surges, Flow. Meas. Instrum. 54 (2017) 136–145, http://dx.doi.org/10.1016/j.flowmeasinst.2017.01.004.
[38] D. Long, N. Rajaratnam, P.M. Steffler, P.R. Smy, Structure of flow in hydraulic jumps, J. Hydraul. Res. 29 (2) (1991) 207–218, http://dx.doi.org/10.1080/00221689109499004.
[39] J.W. Miles, On the generation of surface waves by shear flows, J. Fluid Mech. 3 (2) (1957) 185–204, http://dx.doi.org/10.1017/S0022112057000567.
[40] M. Mossa, On the oscillating characteristics of hydraulic jumps, J. Hydraul. Res. 37 (4) (1999) 541–558, http://dx.doi.org/10.1080/00221686.1999.9628267.
[41] M. Mossa, A. Petrillo, H. Chanson, Tailwater level effects on flow conditions at an abrupt drop, J. Hydraul. Res. 41 (1) (2003) 39–51, http://dx.doi.org/10.1080/00221680309499927.
[42] D. Mouaze, F. Murzyn, J.R. Chaplin, Free surface length scale estimation in hydraulic jumps, J. Fluids Eng. 127 (2005) 1191–1193.
[43] F. Murzyn, H. Chanson, Free-surface fluctuations in hydraulic jumps: experimental observations, Exp. Therm. Fluid Sci. 33 (2009) 1055–1064, http://dx.doi.org/10.1016/j.expthermflusci.2009.06.003.
[44] M. Muste, S. Baranya, R. Tsubaki, D. Kim, H. Ho, H. Tsai, D. Law, Acoustic mapping velocimetry, Water Resour. Res. 52 (5) (2016) 4132–4150, http://dx.doi.org/10.1002/2015WR018354.
[45] G. Nebbia, Su taluni fenomeni alternativi in correnti libere, L'Energ. Elettr., Fasc. I XIX (1942) 1–10 (in Italian).
[46] I. Nezu, Open-channel flow turbulence and its research prospect in the 21st century, J. Hydraul. Eng. 131 (4) (2005) 229–246, http://dx.doi.org/10.1061/(ASCE)0733-9429(2005)131:4(229).
[47] A. Nichols, S. Tait, K. Horoshenkov, S. Shepherd, A non-invasive airborne wave monitor, Flow. Meas. Instrum. 34 (2013) 118–126, http://dx.doi.org/10.1016/j.flowmeasinst.2013.09.006.
[48] A. Nichols, S.J. Tait, K.V. Horoshenkov, S.J. Shepherd, A model of the free surface dynamics of shallow turbulent flows, J. Hydraul. Res. 54 (5) (2016) 516–526, http://dx.doi.org/10.1080/00221686.2016.1176607.
[49] H. Nyquist, Thermal agitation of electric charge in conductors, Phys. Rev. 32 (1) (1928) 110.
[50] A.V. Oppenheim, R.W. Schafer, Discrete-Time Signal Processing, Pearson Higher Education, 2010.
[51] M. Pfister, Discussion on: bubbles and waves description of self-aerated spillway flow, J. Hydraul. Res. 46 (3) (2008) 420–423, http://dx.doi.org/10.1080/00221686.2008.9521877.
[52] S. Pope, Turbulent Flows, Cambridge University Press, 2000.
[53] N.S.L. Rao, H.E. Kobus, Characteristics of Self-Aerated Free-Surface Flows. Water and Waste Water/Current Research and Practice 10 Eric Schmidt Verlag, Berlin, Germany, 1971.
[54] N.S.L. Rao, K. Seetharamiah, T. Gangadharaiah, Characteristics of self-aerated flows, J. Hydraul. Div., ASCE 96 (HY2) (1970) 331–355.
[55] M. Razaz, K. Kawanisi, A. Kaneko, I. Nistor, Application of acoustic tomography to reconstruct the horizontal flow velocity field in a shallow river, Water Resour. Res. 51 (12) (2015) 9665–9678, http://dx.doi.org/10.1002/2015WR017102.
[56] V. Roussinova, N. Biswas, R. Balachandar, Revisiting turbulence in smooth uniform open channel flow, J. Hydraul. Res. 46 (sup1) (2008) 36–48, http://dx.doi.org/10.1080/00221686.2008.9521938.
[57] A.G. Roy, T. Buffin-Bélanger, H. Lamarre, A.D. Kirkbride, Size, shape and dynamics of large-scale turbulent flow structures in a gravel-bed river, J. Fluid Mech. 500 (2004) 1–27, http://dx.doi.org/10.1017/S0022112003006396.
[58] R. Savelsberg, Experiments on Free-surface Turbulence, Technische Universiteit Eindhoven, Eindhoven, 2006, http://dx.doi.org/10.6100/IR609526.
[59] A.B. Schvidchenko, G. Pender, Flume study of the effect of relative depth on the incipient motion of coarse uniform sediments, Water Resour. Res. 36 (2) (2000) 619–628 (doi: 0043-1397/00/1999WR900312).
[60] A.B. Schvidchenko, G. Pender, Macroturbulent structure of open-channel flow over gravel beds, Water Resour. Res. 37 (3) (2001) 709–719, http://dx.doi.org/10.1029/2000WR900280.
[61] C.E. Shannon, Communication theory of secrecy systems, Bell Syst. Tech. J. 28 (4) (1949) 656–715.
[62] A. Tamburrino, J.S. Gulliver, Free-surface visualization of streamwise vortices in a channel flow, Water Resources Research 43 (11) (2007) W11410, http://dx.doi.org/10.1029/2007WR005988.
[63] M.A.C. Teixeira, S.E. Belcher, Dissipation of shear-free turbulence near boundaries, J. Fluid Mech. 422 (2000) 167–191, http://dx.doi.org/10.1017/S002211200000149X.
[64] R.E. Thomas, L. Schindfessel, S.J. McLelland, S. Creëlle, T. De Mulder, Bias in mean velocities and noise in variances and covariances measured using a multistatic acoustic profiler: the Nortek Vectrino Profiler, Meas. Sci. Technol. 28 (7) (2017), http://dx.doi.org/10.1088/1361-6501/aa7273.
[65] L. Toombes, H. Chanson, Surface waves and roughness in self-aerated supercritical flow, Environ. Fluid Mech. 7 (3) (2007) 259–270, http://dx.doi.org/10.1007/s10652-007-9022-y.
[66] D. Valero, D.B. Bung, Hybrid Investigations of Air Transport Processes in Moderately Sloped Stepped Spillway Flows. In: Proceedings of the 36th IAHR World Congress, 28 June–3 July 2015, The Hague, The Netherlands. ISBN: 978-90-824846-0-1, 2015.
[67] D. Valero, D.B. Bung, Development of the interfacial air layer in the non-aerated region of high-velocity spillway flows. Instabilities growth, entrapped air and influence on the self-aeration onset. Int. J. Multiph. Flow. 84 (2016) 66–74, http://dx.doi.org/10.1016/j.ijmultiphaseflow.2016.04.012.
[68] D. Valero, D.B. Bung, Reformulating self-aeration: turbulent growth of the free surface perturbations leading to air entrainment, Int. J. Multiph. Flow. (2017), http://dx.doi.org/10.1016/j.ijmultiphaseflow.2017.12.011.
[69] H. Wang, H. Chanson, Experimental study of turbulent fluctuations in hydraulic jumps, J. Hydraul. Eng. 141 (7) (2015) 04015010, http://dx.doi.org/10.1061/(ASCE)HY.1943-7900.0001010.
[70] H. Wang, H. Chanson, Air entrainment and turbulent fluctuations in hydraulic jumps, Urban Water J. 12 (6) (2015) 502–518, http://dx.doi.org/10.1080/1573062X.2013.847464.
[71] H. Wang, F. Murzyn, Experimental assessment of characteristic turbulent scales in two-phase flow of hydraulic jump: from bottom to free surface, Environ. Fluid Mech. (2016) 1–19, http://dx.doi.org/10.1007/s10652-016-9451-6.
[72] H. Wang, F. Murzyn, H. Chanson, Interaction between free-surface, two-phase flow and total pressure in hydraulic jump, Exp. Therm. Fluid Sci. 64 (2015) 30–41, http://dx.doi.org/10.1016/j.expthermflusci.2015.02.003.
[73] I.R. Wood, Air Entrainment in Free-Surface Flows. IAHR Hydraulic Structures Design Manual No. 4, Hydraulic Design Considerations, Balkema Publ, Rotterdam, The Netherlands, 1991, p. 149.
[74] W.R. Young, C.L. Wolfe, Generation of surface waves by shear-flow instability, J. Fluid Mech. 739 (2014) 276–307, http://dx.doi.org/10.1017/jfm.2013.617.
[75] G. Zhang, H. Chanson, Hydraulics of the developing flow region of stepped spillways. I: physical modeling and boundary layer development, J. Hydraul. Eng. 142 (7) (2016) 04016015, http://dx.doi.org/10.1061/(ASCE)HY.1943-7900.0001138.
[76] G. Zhang, H. Chanson, Self-aeration in the rapidly- and gradually-varying flow regions of steep smooth and stepped spillways, Environ. Fluid Mech. 17 (2) (2017) 20, http://dx.doi.org/10.1007/s10652-015-9442-z.
[77] Q. Zhong, Q. Chen, H. Wang, D. Li, X. Wang, Statistical analysis of turbulent super-streamwise vortices based on observations of streaky structures near the free surface in the smooth open channel flow, Water Resour. Res. 52 (5) (2016) 3563–3578, http://dx.doi.org/10.1002/2015WR017728.